Artificial Ionospheric Layers during Pump Frequency Stepping Near the 4th Gyroharmonic at HAARP

E. Sergeev,[1,2] S. Grach,[1,2] A. Shindin,[1,2] E. Mishin,[3] P. Bernhardt,[4] S. Briczinski,[4] B. Isham,[5] M. Broughton,[6] J. LaBelle,[6] and B. Watkins[7]

[1]*Radiophysical Research Institute, 25a/12 Bolshaya Pecherskaya Street, Nizhny Novgorod 603950, Russia*
[2]*Lobachevsky State University of Nizhny Novgorod, 23 Gagarin Avenue, Nizhny Novgorod 603950, Russia*
[3]*Space Vehicles Directorate, Air Force Research Laboratory, Kirtland AFB, New Mexico 87117, USA*
[4]*Plasma Physics Division, Naval Research Laboratory, Washington, DC 20375, USA*
[5]*Department of Electrical and Computer Engineering, Interamerican University, Bayamón, Puerto Rico 00957, USA*
[6]*Department of Physics and Astronomy, Dartmouth College, Hanover, New Hampshire 03755, USA*
[7]*Geophysical Institute, University of Alaska Fairbanks, Fairbanks, Alaska 99775, USA*
(Received 14 September 2012; published 5 February 2013)

We report on artificial descending plasma layers created in the ionosphere F region by high-power high-frequency (HF) radio waves from High-frequency Active Auroral Research Program at frequencies f_0 near the fourth electron gyroharmonic $4f_{\rm ce}$. The data come from concurrent measurements of the secondary escaping radiation from the HF-pumped ionosphere, also known as stimulated electromagnetic emission, reflected probing signals at f_0, and plasma line radar echoes. The artificial layers appeared only for injections along the magnetic field and $f_0 > 4f_{\rm ce}$ at the nominal HF interaction altitude in the background ionosphere. Their average downward speed $\sim$0.5 km/s holds until the terminal altitude where the local fourth gyroharmonic matches f_0. The total descent increases with the nominal offset $f_0 - 4f_{\rm ce}$.

DOI: 10.1103/PhysRevLett.110.065002 PACS numbers: 94.20.Tt, 52.25.Os, 52.50.Qt

High-power high-frequency (HF) radio beams (pump waves) of ordinary (O) polarization transmitted from the ground into the ionosphere excite plasma eigenmodes, e.g., Langmuir and upper hybrid (UH), due to parametric instabilities [1–5]. The pump-plasma interaction is strongest between the reflection height h_r, where the plasma frequency $f_{\rm pe}$ matches the pump frequency f_0, and heights slightly below the upper hybrid resonance height $h_{\rm uh}$ where $f_0 = f_{\rm uh} = [f_{\rm pe}^2 + f_{\rm ce}^2]^{1/2}$ (the UH resonance frequency). The excited plasma waves generate secondary or stimulated electromagnetic emissions (SEE) [6] via conversion of the plasma modes into electromagnetic waves (see e.g., Ref. [7]) and accelerate electrons up to a few tens of eV (e.g., Ref. [8]). The accelerated electrons cause optical emissions (artificial airglow) and can ionize neutral gas if their energy exceeds 12–18 eV [8–11].

The upgraded High-frequency Active Auroral Research Program (HAARP) heating facility situated near Gakona, Alaska (62.4° N, 145.15° W, magnetic dip angle $\theta = 14.2°$) provides enough power to produce artificial ionospheric ionization [12,13]. The original experiments [12] employed $f_0 \approx 2f_{\rm ce}$, and artificial ionospheric plasma layers were observed descending by tens of kilometers below the nominal interaction altitude in the background F2-region ionosphere. Their creation was explained [14,15] in terms of an ionizing wave front created due to electron acceleration by strong Langmuir turbulence generated by the O-mode pump wave in the critical layer near h_r. It is also found [13] that production of artificial plasma layers is optimized for f_0 slightly below the double resonance frequency f_d, at which $2f_{\rm ce}$ matches $f_{\rm uh}$. This suggests the importance of O-UH wave coupling. Determining the effects of both Langmuir and upper hybrid interactions is critical for understanding the mechanism of electron acceleration creating artificial ionospheric plasmas.

This Letter reports artificial ionospheric layers created at HAARP for f_0 near the fourth electron gyroharmonic. The data include measurements of SEE and diagnostic HF radio reflections at three separate sites and enhanced magnetic field-aligned plasma line (PL) radar echoes by the modular UHF incoherent scatter radar (MUIR) located at HAARP.

The experiment was run on 28 March, 2011 between 1500 and 1600 AST. The HF beam was pointed vertically (V) during the first 30 min and toward the magnetic zenith (MZ), i.e., along the geomagnetic field, thereafter. Injections of O-mode pump waves were made at full pump power $P_0 \approx 1.8$ GW ERP (effective radiated power), and pump frequencies f_0 ranging from 5730 to 5880 kHz, stepping by 30 kHz every 5 min. Each 5-min interval was comprised of three pumping periods followed by 30 s off.

The first and third periods consisted of low-duty pulses of duration $\tau_p = 20$ ms and an interpulse period $T_p = 1$ s (mode p), for a total of 30 and 180 s, respectively. The second period consisted of $\tau_q = 160$ ms pulses separated by 40-ms pauses (mode q of $T_q = 0.2$ s), for a total of 1 min. In order to monitor the pump wave absorption and reflection altitude, short diagnostic pulses of length

$\tau_d = 100\ \mu$s, of the same power and frequency as the pump wave, were also transmitted 20 ms prior each mode p pulse and in the middle of each mode q pause. Note the difference in average radiated power $\bar{P}_{p,q} \approx P_0\tau_{p,q}/T_{p,q}$ between mode p ($\approx$0.036 GW ERP) and mode q ($\approx$1.44 GW ERP).

The background ionosphere was monitored by the HAARP DPS-4D ionosonde during the 30-s off periods. The critical frequency f_{OF2} was $\approx$6.2–6.5 MHz, so the pump nominal reflection altitude h_r^* was $\approx$ 210–220 km. The observational sites were located along the meridian to the south of the HAARP facility at (A) Riverview Lodge (about 11 km distant), (B) Tonsina River Lodge (83 km), and (C) Tiekel River Lodge (113 km). Site A (B) was nearly under the heated region during injections at vertical (MZ). A 30-m folded-dipole BWDS antenna was used in site A, an AS-2259/GR inverted-V antenna was used at site B, and a 10-m^2 diamond magnetic loop was used at site C. The receiver at A (B and C) digitized a band of 250 (300–400) kHz around the pump frequency. The dynamic range of the instruments after spectral processing is estimated to be better than 90 dB. Despite the differences in the receiving systems, the main features of the SEE and diagnostic reflections observed at each site are virtually the same. The results shown below from site B are representative of all three sites.

Overall, the low-duty pumping periods 1 and 3 (mode p) produced only downshifted emissions, i.e., $\Delta f = f - f_0 < 0$. The nearly continuous pumping during period 2 (mode q) produced well-known downshifted and upshifted features, i.e., the downshifted maximum (DM) at $\Delta f_{\mathrm{DM}} \approx -10$ kHz and broad upshifted maximum (BUM)

$$\Delta f_{\mathrm{BUM}} = f_{\mathrm{BUM}} - f_0 \approx f_0 - s f_{\mathrm{ce}} + \delta f, \tag{1}$$

where s is the harmonic number and $\delta f \approx$ 15–20 kHz (see e.g., Refs. [16–23]). According to the purpose of this Letter, we will focus on the SEE dynamics only during period 2 (mode q).

Figure 1 presents SEE frequency-time spectrograms at site B for vertical and MZ injections. Each spectrogram is obtained using a 130-ms window centered at the 95th ms within each τ_q pulse, with a frequency (time) resolution of 200 Hz (0.2 s). As the BUM exists only at $f_0 > s f_{\mathrm{ce}}$ ($s \geq 3$) and $f_{\mathrm{BUM}} > f_d$ and the BUM feature is seen at $f_0 \geq 5760$ kHz, we conclude that $5730 < 4 f_{\mathrm{ce}} < 5760$ kHz in the interaction region. Furthermore, the absence of the DM for $f_0 = 5760$ kHz indicates that the DM frequency matches the double resonance, i.e., $f_{\mathrm{DM}} \approx 4 f_{\mathrm{ce}} \approx f_{\mathrm{uh}}$ [18,21]. For a given pump frequency, this occurs at a unique altitude h_d. Using the IGRF-11/2010 geomagnetic field model for $f_{\mathrm{ce}}(h)$ and taking $4 f_{\mathrm{ce}}(h_d) \approx f_{\mathrm{uh}}(h_d) \approx f_{\mathrm{DM}} \approx 5750$ kHz gives $h_d \approx 203$ km at MZ.

As seen in Figure 1, the initial stage appears virtually the same for V and MZ injections. However, later in the heating, the development of the BUM differs significantly.

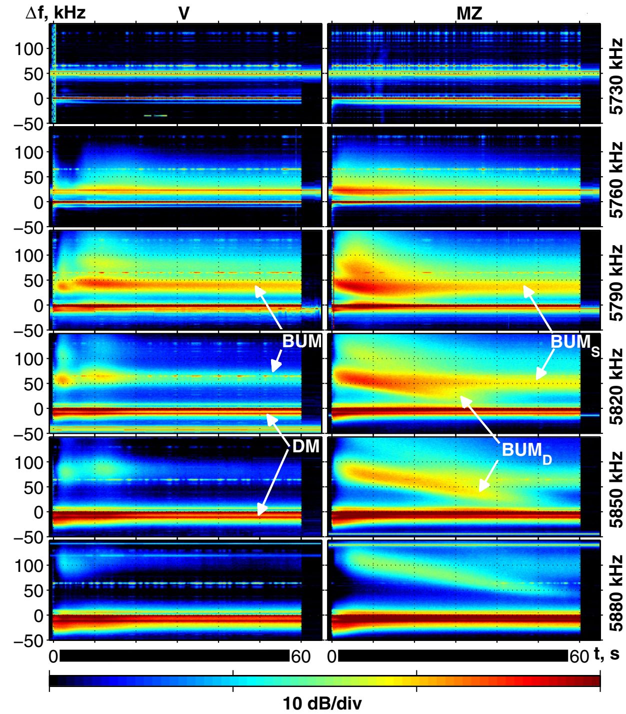

FIG. 1 (color online). SEE frequency-time spectrograms at site B for the V (left column) and MZ (right) directions at different pump frequencies (shown to the right of the spectrograms). The time (frequency) axis origin is at the start of period 2 (the pump frequency f_0). Color codes for the SEE intensity in log scale are given at the bottom. The arrows indicate the DM and BUM features. The black bars indicate period 2.

Not only are the spectra at MZ more intense and broader but the BUM spectrum is also divided into two distinct features, hereafter called BUM$_S$ (S for stationary) and BUM$_D$ (D for descending). The BUM$_S$ does not drift in frequency, the same as the BUM for V injections. The new component, BUM$_D$, drifts with time towards f_0 until its frequency offset Δf_D reaches the minimum $\approx \delta f$ [see Eq. (1)], which is close to the so-called BUM cutoff (see, e.g., Ref. [23]). The cutoff time t_1^* amounts to $\approx$5, 10, 30, and 40 s for $f_0 = 5760$, 5790, 5820, and 5850 kHz, respectively, and exceeds 60 s (the duration of period 2) for $f_0 = 5880$ kHz. However, the frequency drift rate r_f is $\approx$1.2–1.4 kHz/s for all f_0.

Figure 2 details successive SEE spectra 5 s apart for $f_0 = 5850$ kHz. Dashed lines correspond to the BUM$_S$ and BUM$_D$ peaks. The stationary quality of the BUM$_S$ after $\approx$10 s and the drift of the BUM$_D$ peak toward f_0 are evident. After the drift stops at $t \approx t_1^*$, the offset $\Delta f_D \approx \delta f$ remains, while the BUM$_D$ magnitude decreases to the background at $t_2^* = t_1^* + \delta t$, where $\delta t \approx$ 7–12 s.

We interpret these results by employing Eq. (1) and the fact that the BUM exists only for $f_0 > 4 f_{\mathrm{ce}}$. According to Eq. (1), the decrease of Δf_D with time suggests the increase of $f_{\mathrm{ce}}(h(t))$ and hence the descent of the BUM$_D$ generation region. Using the IGRF-11/2010 model for

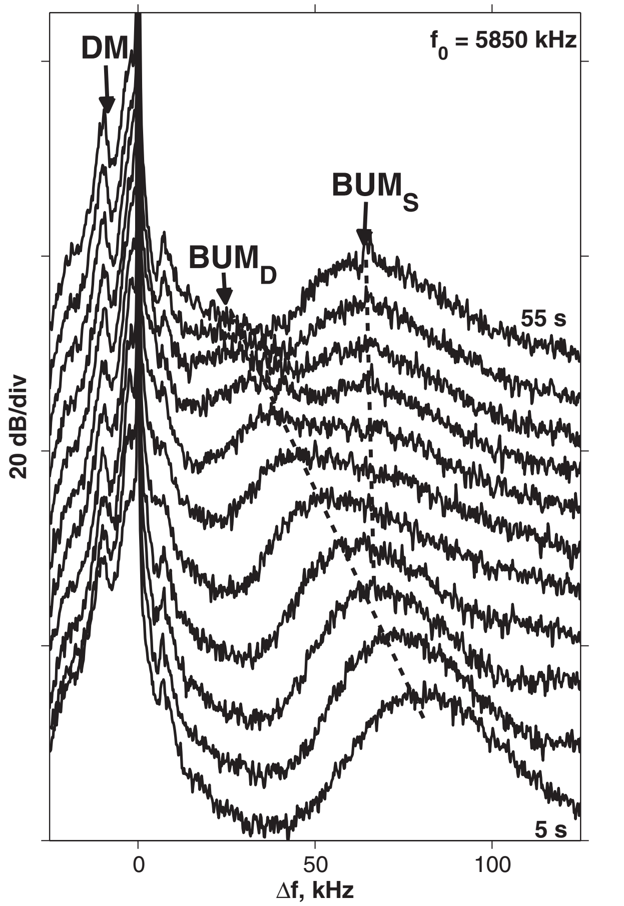

FIG. 2. A sequence of SEE spectra for 5850 kHz pumping, from 5 to 55 s after the start of period 2, with a 5-s time step between spectra. Successive spectra are shifted by 5 dB. Dashed lines show positions of the BUM_S and BUM_D peaks.

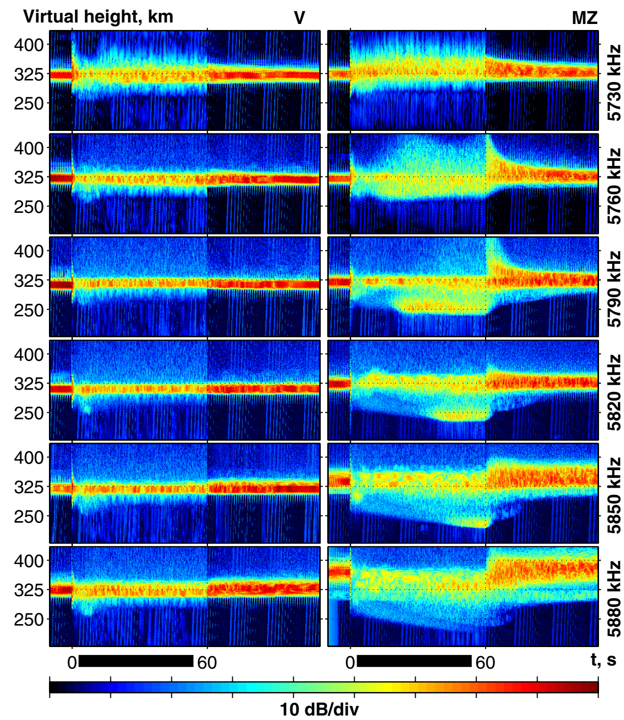

FIG. 3 (color online). The virtual heights of reflected or scattered diagnostic pulses detected at site B during injections at V (left column) and MZ (right). Color codes for the diagnostic signal intensity in log scale are given at the bottom of the figure. The black bars indicate period 2.

$f_{\mathrm{ce}}(h)$ gives the speed of descent $V_{\mathrm{BUM}} \approx r_f(4df_{\mathrm{ce}}/dh)^{-1} \approx 450$–$520$ m/s. The terminal altitude h_2^* where the BUM_D disappears (at t_2^*) corresponds to the double resonance h_d or $f_0 \approx 4f_{\mathrm{ce}}(h_2^*)$. The increase of the overall descent $\Delta h_2^* = V_{\mathrm{BUM}} t_2^*$ with f_0, i.e., $\Delta h_2^* \approx 5 \rightarrow 26$ km for $f_0 = 5760 \rightarrow 5850$ kHz, is defined by the decrease of $h_d(f_{\mathrm{ce}})$. Note that these are the first observations of height-splitting (BUM_S and BUM_D) of the BUM spectrum.

The descent of the BUM_D generation region is consistent with that of the reflection layer of the 100-μs diagnostic pulses. Figure 3 shows variations of the virtual reflection height $h_{\mathrm{v}} = c\delta\tau/2$ of diagnostic pulses reflected or scattered from the $F2$ region and observed at site B. Here, $\delta\tau$ is the time delay and c is the speed of light. The main feature during periods 1 and 3 (mode p) was reflection from the background $F2$ layer centered at $h_{\mathrm{v}} = h_{\mathrm{BF}} \approx 325$ km. It is hereafter referred to as the BF reflection or BF. During period 2, the BF signal suffers absorption, and there also appeared to be diffuse scattering, mostly above h_{BF} for the V injections.

Similar to the SEE features, there is a stark difference between the V and MZ injections above $4f_{\mathrm{ce}}$. Most notable is the development of the layers of scattered or reflected signals below h_{BF} at MZ. Their virtual altitude h_{DL} (DL for descending layers) descends with time well below h_{BF} for $f_0 \geq 5760$ kHz. From Figure 3 it is seen that the decrease of h_{DL} stops near the BUM_D cutoff time t_1^*. After that, the magnitude of the DL signal increases by nearly 50 dB and at $t \approx t_2^*$ attains the BF magnitude. The overall virtual descent Δh_{DL} increases with f_0, that is, $\Delta h_{\mathrm{DL}} \approx 50 \rightarrow 145$ km for $f_0 = 5760 \rightarrow 5880$ kHz, respectively. After the start of period 3, i.e., switching back to the low-duty mode p, the lower layer (the DL) disappeared in a few seconds, and the BF magnitude recovered to that of period 1. Thus, the nearly continuous pumping at MZ for $f_0 > 4f_{\mathrm{ce}}$ results in two distinct layers of reflection, i.e., BF and DL.

The concurrent MUIR observations of descending layers of enhanced PL echoes (cf. Ref. [14]) agree with the $\mathrm{DL}/\mathrm{BUM}_D$ characteristics. Figure 4 shows the altitude dependence of the PL echo intensity, as seen by the MUIR with the altitude resolution of 600 m. The PL signal was integrated for 0.5 s. The radar was turned on about 20 s after the start of period 2 for 5820 kHz at MZ. The PL echoes are clearly seen near the nominal reflection altitude (BF), 210–220 km, during periods 1 and 3. However,

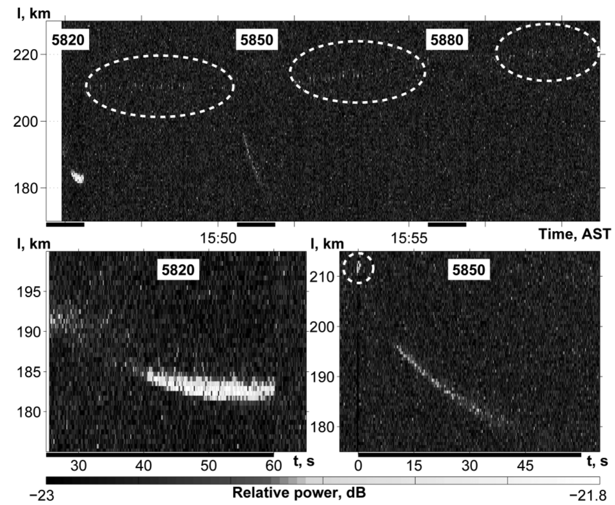

FIG. 4. (top) Relative power of PL echoes from the MUIR vs distance $l \approx h/\cos(14.2°)$ during the last three intervals of period 2 at MZ. (bottom) Zoomed images for $f_0 = 5820$ (left) and 5850 (right) kHz. Black bars indicate period 2. Dashed lines encircle the enhanced PL echoes during periods 1 and 3, near h_r, and at the onset of period 2. The radar was turned on about 20 s after the start of period 2 for 5820 kHz.

during period 2 the PL echo altitude decreases by about 30 km. The descent ends at the BUM$_D$ cutoff time t_1^*, and furthermore, the PL intensity for 5820 kHz (5850 kHz) significantly increases (decreases) until the end of period 2. Note that the PL echo intensity for 5850 kHz peaks near the nominal reflection altitude at the onset of period 2 and the PL echo at 5880 kHz was not detected during period 2.

The speed of descent of the PL echo for 5820 and 5850 kHz is 460–600 m/s, i.e., close to $V_{\rm BUM}$. At the PL terminal altitude $h_{\rm PL} \approx 180(177)$ km for 5820 (5850) kHz, the total descent is $\approx 27(30)$ km and $4f_{\rm ce}(h_{\rm PL}) \approx f_0$. This is close to the overall descent of the BUM$_D$, Δh_2^*, which is about 20 and 26 km for 5820 and 5850 kHz, respectively. Slight differences between the plasma line and SEE results can be attributed to the different regions of generation of the PL echo and the BUM. The PL echo region can be at the O-mode critical height or the radar matching height slightly below [24], while the BUM's is likely well below (near) the UH resonance layer at large (small) offsets $f_0 - 4f_{\rm ce}$ [21].

Descending layers appear only during injections along the magnetic field at $f_0 > 4f_{\rm ce}$ at the nominal interaction altitude in the background ionosphere. The same asymmetry has been observed [8] in the airglow enhancement at 427.8 nm from the $N_2^+(B^2\Sigma_u^+)$ state (18.75 eV threshold) but not at 630.0 nm (1.96 eV threshold) nor in the T_e enhancement. This observation suggests that the mechanism of the acceleration of high-energy electrons differs from that for the heating and acceleration of low-energy electrons. Since the 427.8-nm emission indicates ionization, we conclude that the descending layers are produced mainly by the acceleration of electrons to energies of a few tens of eV (cf. Refs. [14,15]).

Finally, the speed of descent exceeds that for $2f_{\rm ce}$ [12,13] by 2–3 times. This can be attributed to a more efficient electron acceleration due to (i) higher HF pump power $P_0 \sim f_0^2$ and (ii) existing photoelectrons that can be accelerated much more efficiently than thermal electrons (cf. Ref. [25]). The sensitivity to the sign of the offset $f_{\rm uh} - 4f_{\rm ce}$ indicates the important role of upper hybrid waves (e.g., Refs. [8,21]). However, the fact that the descent starts during the first few pulses of period 2, i.e., before UH-induced anomalous absorption can develop, and the presence of enhanced descending PL echoes also indicate the significance of Langmuir turbulence.

HAARP is a DoD program operated jointly by the U.S. Air Force and U.S. Navy. E. S., S. G., and A. S. were supported by EOARD/AFOSR and RFBR Grants No. 11-02-00125-a and No. 12-02-00513-a and the Ministry of Education and Science of the Russian Federation, Project No. 14.132.21.1434. E. M., P. B. and S. B., and B. I. were supported by AFOSR, ONR, and ARO Grant No. W911NF-11-1-0217, respectively.

[1] F. W. Perkins, C. R. Oberman, and E. J. Valeo, J. Geophys. Res. **79**, 1478 (1974).
[2] Y. I. Al'ber *et al.*, Sov. Phys. JETP **39**, 275 (1974).
[3] D. F. DuBois, A. H. Rose, and D. Russel, J. Geophys. Res. **95**, 21221 (1990).
[4] S. M. Grach, A. N. Karashtin, N. A. Mityakov, V. O. Rapoport, and V. Yu. Trakhtengerts, Radiophys. Quantum Electron. **20**, 1254 (1977).
[5] V. V. Vas'kov and A. V. Gurevich, Sov. Phys. JETP **46**, 487 (1977).
[6] B. Thidé, H. Kopka, and P. Stubbe, Phys. Rev. Lett. **49**, 1561 (1982).
[7] S. M. Grach, Radiophys. Quantum Electron. **28**, 470 (1985).
[8] B. Gustavsson, T. Leyser, M. Kosch, M. Rietveld, Å. Steen, B. Brändström, and T. Aso, Phys. Rev. Lett. **97**, 195002 (2006).
[9] M. J. Kosch, T. Pedersen, M. T. Rietveld, B. Gustavsson, S. M. Grach, and T. Hagfors, Adv. Space Res. **40**, 365 (2007).
[10] V. V. Vas'kov *et al.*, JETP Lett. **34**, 557 (1981).
[11] S. M. Grach, G. Komrakov, M. Yurishchev, B. Thidé, T. Leyser, and T. Carozzi, Phys. Rev. Lett. **78**, 883 (1997).
[12] T. Pedersen, B. Gustavsson, E. Mishin, E. Kendall, T. Mills, H. C. Carlson, and A. L. Snyder, Geophys. Res. Lett. **37**, L02106 (2010).
[13] T. Pedersen, M. McCarrick, B. Reinisch, B. Watkins, R. Hamel, and V. Paznukhov, Ann. Geophys. **29**, 47 (2011).
[14] E. Mishin and T. Pedersen, Geophys. Res. Lett. **38**, L01105 (2011).
[15] B. Eliasson, X. Shao, G. Milikh, E. Mishin, and K. Papadopoulos, J. Geophys. Res. **117**, A10321 (2012).
[16] M. Ashrafi, M. J. Kosch, K. Kaila, and B. Isham, J. Geophys. Res. **112**, A05314 (2007).

[17] T. D. Carozzi, B. Thidé, S. M. Grach, T. B. Leyser, M. Holz, G. P. Komrakov, V. L. Frolov, and E. N. Sergeev, J. Geophys. Res. **107**, 1253 (2002).
[18] E. Sergeev, V. Frolov, S. Grach, and P. Kotov, Adv. Space Res. **38**, 2518 (2006).
[19] V. L. Frolov, S. M. Grach, L. M. Erukhimov, G. P. Komrakov, E. N. Sergeev, B. Tide, and T. Carozzi, Radiophys. Quantum Electron. **39**, 241 (1996).
[20] V. L. Frolov, L. Ekukhimov, L. Kagan, G. Komrakov, E. Sergeev, and P. Stubbe, Phys. Rev. Lett. **81**, 1630 (1998).
[21] S. M. Grach, E. N. Sergeev, V. A. Yashnov, and P. V. Kotov, Radiophys. Quantum Electron. **51**, 499 (2008).
[22] T. B. Leyser, Space Sci. Rev. **98**, 223 (2001).
[23] T. B. Leyser, B. Thidé, M. Waldenvik, S. Goodman, V. L. Frolov, S. M. Grach, A. N. Karashtin, G. P. Komrakov, and D. S. Kotik, J. Geophys. Res. **98**, 17597 (1993).
[24] M. T. Rietveld, B. Isham, H. Kohl, C. La Hoz, and T. Hagfors, J. Geophys. Res. **105**, 7429 (2000).
[25] E. Mishin, W. Burke, and T. Pedersen, J. Geophys. Res. **109**, A02305 (2004).